Microlenses fabricated by two-photon laser polymerisation for intravital cell imaging with non-linear excitation microscopy

M. Marini[1,+], A. Nardini[3,+] , R. Martínez Vázquez[2,+], C. Conci[3], M. Bouzin[1], M. Collini[1], R. Osellame[2], G. Cerullo[4], B.S. Kariman[4], M. Farsari[5], E. Kabouraki[5], M.T. Raimondi[3,+,*] , G. Chirico[1,+,*].

1 Department of Physics, Università degli Studi di Milano-Bicocca, Piazza della Scienza 3, 20126, Milan, Italy
2 Institute for Photonics and Nanotechnologies (IFN), CNR, Piazza L. da Vinci 32, 20133 Milan, Italy
3 Department of Chemistry, Materials and Chemical Engineering "Giulio Natta", Politecnico di Milano, Piazza L. da Vinci 32, 20133 Milan, Italy
4 Department of Physics, Politecnico di Milano, Piazza L. da Vinci 32, 20133 Milan, Italy
5 FORTH/IESL, N. Plastira 100, 70013, Heraklion, Greece.

+: contributed equally to the work
*: corresponding authors.

Keywords: 3Dl micro scaffolds, two-photon polymerization, microlenses, two-photon imaging, confocal microscopy, SZ2080.

Abstract.
Non-linear excitation microscopy offers a number of advantages for *in vivo* imaging compared to conventional confocal techniques. However, tissue penetration can still be an issue due to both scattering and spherical aberrations induced on highly focused beams by the tissue. The use of low numerical aperture objectives to pass through the outer layers of the skin, together with high dioptric power microlenses implanted in-vivo close to the observation volume, can be beneficial to the reduction of the optical aberrations. Here, we develop and test, on a monolayer of fibroblast cells, plano-convex micro-lenses to be used for non-linear imaging of biological tissue. The microlenses can be used as single lenses or multiplexed in an array. A thorough test of the wave front of the lenses is reported together with their modulation transfer function and wave front profile. Notably, we could retrieve magnified fluorescence images through the microlenses coupled to commercial confocal and two-photon excitation raster scanning microscopes. The signal to noise ratio of the images is not substantially affected by the use of the microlenses and the magnification can be adjusted by the relative position of the microlens array to the microscope objective and the immersion medium. These results are opening the way to the application of implanted micro-optics for optical in-vivo inspection of biological processes.

1. Motivation/introduction

In vivo observation of tissue is desirable in many fields, from immunology[1,2] to the assessment of the foreign body reaction as a test of immunogenicity to biomaterials[3,4]. To date, different kinds of imaging windows have been developed and used[5] in combination with fluorescence microscopy. However, the majority of the existing optical windows influence and/or have a severe impact on the laboratory animal health and behavior, therefore limiting the medical relevance of the observations. We recently proposed a miniaturized (500 µm × 500 µm × 100 µm) imaging window, named Microatlas, which incorporates an array of micro-scaffolds, able to guide the regeneration of tissue at the interface with the implanted material[6]. Although the Microatlas has been validated up to now in embryonated chicken eggs[6], it can also be implanted sub cute in mice, in which case non-linear excitation microscopy would be the best choice for direct imaging. Non-linear excitation microscopy with near infrared (NIR) laser sources can mitigate the penetration issues in tissues[7–9] by reducing the effect of scattering on the point spread function. However, the reduction of scattering with wavelength is decreasing with a lower than fourth power law in animal tissues[10], and the spatial resolution of images in deep tissue is also limited by spherical aberrations. These beam aberrations arise simply from the propagation of the high numerical aperture beam through the different layers of the animal skin. Instead of imaging implanted scaffolds by means of the long working distance and high numerical aperture objective of an external microscope, our long term purpose is to develop a set of microlenses that will be coupled directly to the micro scaffolds, implanted *in vivo*, and used to enable non-linear imaging of the tissue regenerated within the micro scaffolds, by focusing collimated beams right at the site of observation. Structuring of these microlenses directly on top of the micro scaffolds would then reduce the tissue-induced spherical aberrations and allow longitudinal studies of tissue regeneration *in vivo*. In order to image micro scaffolds extending $\simeq 100\ \mu m$ along the optical axis, we would need to fabricate microlenses with high curvature and smooth surface, and this is a particularly demanding task. Among additive manufacturing (AM) techniques, the only suitable technology to achieve this goal is two-photon polymerization (2PP)[11–15].

In this framework, microlenses have already been developed and fabricated by 2PP, and tested for transmission imaging. From the very first study in this field[16], attention was drawn to the optimization of the optical quality of the surface, by reducing the fabrication thickness[17], or by changing the fabrication scanning path[16]. In this previous work, the microlenses, also in the form of an array, were tested for conventional transmission imaging. More recently, the optical characterization has encompassed the study of the Modulation Transfer Function (MTF), which is an indirect measure of the aberrations. For example, the group of Giessen[18] fabricated multi-microlens systems, and characterized them thoroughly for axial and nonaxial aberrations. In a complementary study, the same group achieved the fabrication of free-form optical components directly on top of optical fibers for endoscopy[19]. In the same field of endoscopy, Li et al.[17] demonstrated the feasibility of 2PP of microlenses for optical coherence tomography (OCT) probes. However, to our knowledge, no attempt has been made to test microfabricated lenses under the more demanding signal/noise ratio conditions of fluorescence imaging or, even more demanding, in the case of non-linear excitation microscopy of biological samples.

The present work is specifically devoted to the design and simulation of microlenses for two-photon excitation microscopy, to the development of methods and protocols for their fabrication and to their experimental testing on cell imaging. We choose here 2PP to enable the fabrication of the microlenses surfaces with arbitrary shape at high resolution, and develop and test a scanning protocol that, based on a random polar scanning and a combination of laser and UV lamp polymerization, minimizes the surface roughness and simultaneously increases the fabrication throughput. We further fully characterize the microlenses for wide field transmission and fluorescence imaging and for confocal and two-photon scanning microscopy. These microlenses can be included in implantable devices for the direct inspection of cellular dynamics *in vivo*[6] or in integrated in microfluidic setups for the *in vitro* monitoring of complex biosystems, such as organoids, directly in the organoid bioreactor.

2. Results and discussion

2.1 Microlenses design

The microlenses imply the use of collimated (or almost collimated) light. This is motivated by the rationale of this study, i.e. the use of a microlens or an array of microlenses right at the site of observation, typically an implanted micro scaffold, collecting and focusing a collimated beam.

The skin of a laboratory animal, like a rodent, is composed of several layers[20], partly made of muscle and partly of adipose tissue. Sebaceous glands and hair follicles, being obstacles larger than the light wavelength, give rise to complex diffraction patterns and also to beam attenuation. Instead, smaller components of the tissue give rise to diffuse scattering, whose effect on imaging can be reduced by adopting a recently developed heterodyne measurement and phase-conjugation correction of the scattered field[21,22]. Apart from these correction strategies, which are not the subject of this work, we notice that different skin layers are endowed with different refractive index values. In fact, the refractive index slightly changes among various tissues, being approximately equal to[10] $n \simeq$1.38-1.39 at $\lambda \simeq 630\,nm$ with the exception of adipose tissue that has $n \simeq 1.42$. The refractive index of the tissues decreases substantially with increasing wavelength [see Bolin et al.[10] and, **Fig.SI1**] according to a power law $\approx \lambda^{-1.5}$ over the range $400\,nm < \lambda < 700\,nm$, passing from $n \simeq$ 1.491 at $\lambda = 400\,nm$ to $n \simeq$ 1.395 at $\lambda = 700\,nm$. No data are available yet in the near infrared region typically used for non-linear excitation ($\lambda \geq 800\,nm$). However, from the data in Bolin et al.[10] we can estimate for the muscle $n \simeq$ 1.392 at $\lambda = 800\,nm$ (**Fig.SI1**). As a matter of fact, microlenses implanted subcute in mice will be probably embedded in the “panniculus carnosus”, similar to muscle, denser but with a lower refractive index than fat. All these considerations imply that the microlenses will be working in an environment having a refractive index about 30% higher than that of air, where lenses are typically tested in optical studies. Therefore, larger curvature of the optical surfaces or even a larger refraction index should be used for the fabrication of our microlenses.

An example of the spherical aberrations observed with high numerical aperture optics in an inhomogeneous medium is simulated in **Fig. 1A**. The propagation medium is either pure water (refraction index $n_1 \simeq 1.34$ at $\lambda = 0.8\,\mu m$) or composed of two slabs of materials of thickness $8\,mm < d_1 < 10mm$ ($n_1 \simeq 1.34$) and $d_2 = f_{FFL} - d_1$ (with refractive index $n_2 = 1.45$; f_{FFL} is the front focal length). The test was performed on a plano-aspherical lens, 25.4 mm in size with curvature radius 12.6 mm (see **SI1** for details), optimized for propagation in water and a pupil size of 10 mm. The aberrations induced on the wave front when increasing the pupil size and/or changing the composition of the propagation medium are primarily spherical and can be characterized by the Zernike polynomial[23] ${Z_4}^0$. The ${Z_4}^0$ amplitude, $a_{4,0}$, depends steeply on the pupil size for size larger than 10-15 mm (**Fig.1B**). The spherical aberration coefficient increases more steeply for the propagation in the inhomogeneous medium ($d_1 = 8\,mm$) than in pure water (**Fig.1B**) and arises from the mismatch in the refractive indices in the propagation medium as indicated by the linear dependence of $a_{4,0}$ on the refractive index n_2 (**Fig.1A**) and on the thickness d_2 of the high refractive index slab (**Fig.1B**, inset). The possibility to obtain the tight focusing of a Gaussian laser beam needed for non-linear excitation microscopy is therefore limited by the propagation in inhomogeneous media. This drawback can be overcome by the use of microlenses implanted close to the observation field.

Aiming at the development of methods and protocols for rapid prototyping of microlenses with the optical quality needed to prime non-linear excitation, we focus here on the simplest case of a refractive lens, i.e. a plano-convex lens with a pedestal, fabricated on top of a supporting borosilicate glass slide (thickness $\simeq 170\,\mu m$, **Table I**). The plano-convex lens is a good approximation of the shape that theoretically minimizes the spherical aberrations for collimated light[24]. The geometrical design parameters of the lens are reported in **Table I** together with a sketch of the microlens and the location of its principal planes.

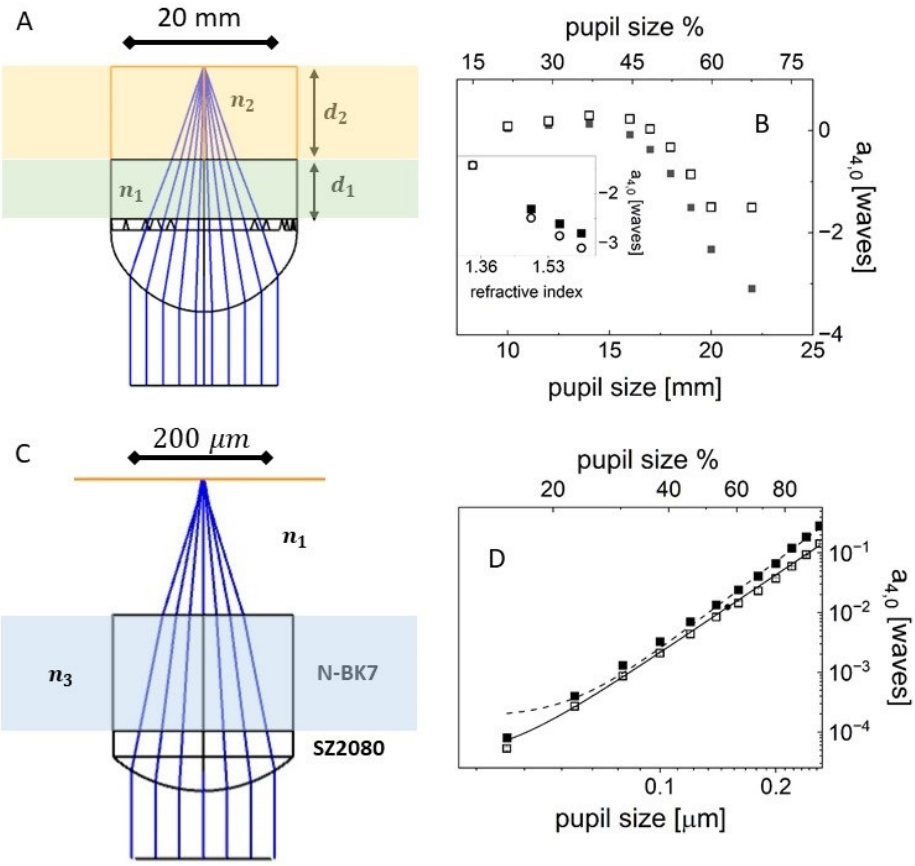

Figure 1. Simulation of the spherical aberrations arising on highly collimated beams when passing through an inhomogeneous sample ($\lambda = 0.8\,\mu m$). **A:** sketch of a macroscopic plano-aspherical lens working in a homogenous medium (refractive index $n_1 = 1.3395$) or in an inhomogeneous medium (refractive indices are $n_1 = 1.34$ and $n_2 = 1.45$, $8mm < d_1 < 10\,mm, d_2 = f_{FFL} - d_1$). **B**: spherical aberration coefficient $a_{4,0}$ as a function of the pupil size for propagation in homogeneous (open squares) or inhomogeneous medium (filled squares, d_1 = 8 mm). Inset: dependence of $a_{4,0}$ as a function of the n_2 refractive index ($d_1 = 8mm$ open squares; $d_1 = 10mm$ filled squares). **C**: diagram of a single plano-convex microlens (diameter = 264 μm) fabricated on a N-BK7 glass substrate ($170\,\mu m$ < thickness < $230\,\mu m$). Tissue is approximated with sea water ($n_1 = 1.34$). **D**: spherical coefficient $a_{4,0}$ as a function of the microlens pupil size, p, in air (filled squares) and in water (open squares). The solid and the dashed lines are the best fit to the data to a power law $a_{4,0} \propto p^{-4.3\pm0.3}$.

An example of the design of a plano-convex microlens with diameter 264 μm is reported in **Fig.1C** for axial illumination. This microlens allows wide-field imaging with a field of view of $\simeq 250\,\mu m$ (see **SI5, "Field of view of microlenses"**). In order to image wider fields of view, these microlenses could be assembled in a microarray. The plano-convex lens reported in **Fig.1C** has a longitudinal spherical aberration (LSA) ≤ 5 μm in axis and LSA ≤ 20 μm for a beam angle $\theta = 6^o$ with respect to the optical axis (that corresponds to a field of view under

scanning $\simeq 35\,\mu m$). The maximum Optical Path Difference is $\simeq 1.5$ waves (mostly below 1 wave, unless for the marginal rays of the tilted beam, see **Fig.SI2.1**).

Table I: geometrical parameters of the plano-convex microlens.

surface	curvature radius $[\mu m]$	thickness $[\mu m]$	material	refractive index $[\lambda = 0.8\,\mu m]$	radius $[\mu m]$	sketch
1	200.0	50.0	SZ2080	n= 1.46*	132.0	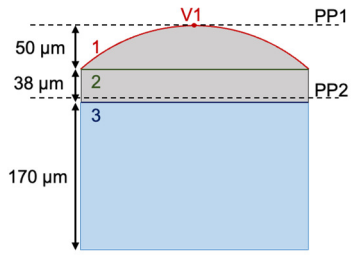
2	∞	38.0	SZ2080	n= 1.46*	132.0	
3	∞	170.0	N-BK7	n= 1.51	132.0	

Geometrical parameters for a plano-convex lens microfabricated in SZ2080. The effective front focal length in air is $f_{FFL} \simeq 164\,\mu m$. The two principal planes (PP, dashed lines in the sketch) lie at the vertex V1 and $36\,\mu m$ below surface 2. *from Žukauskas et al.[25].

The beam focused by the microlens is slightly aberrated even by using the maximum pupil size $\simeq 260\,\mu m$, as can be judged from the intensity profile of a Gaussian beam simulated at the microlens focal plane (**Fig.SI2.2B**) where we can estimate a beam waist ($1/e^2$ radius) of $(1.20 \pm 0.03)\,\mu m$ at $\lambda = 0.8\,\mu m$ (**Fig.SI2.2**), a value only 2-3 times larger than the one typically used for two-photon excitation in biological samples. The aberrations on the wave front can be quantified at the focal plane of the microlens (the plane of the circle of minimum confusion) in terms of the Zernike polynomials: we find again that the major contribution for axial propagation is the spherical one corresponding to the Zernike polynomial[23] ${Z_4}^0$. The $a_{4,0}$ coefficient increases steeply as a power law with exponent $\simeq 4$ (**Fig.1D**), as expected for the thin lens treatment[24]. The spherical aberrations resulted slightly larger when the microlens is focusing in air (**Fig.1D**, filled symbols) rather than in water (**Fig.1D**, open symbols), due to index matching at the exit pupil.

2.2 Fabrication and characterization by scanning electron microscopy (SEM)

Following the simulations reported in the previous section, we decided to fabricate plano-convex lenses by 2PP of the SZ2080 photoresist, a biocompatible photosensible material[25]. Single plano convex lenses, or an hexagonal microarray of these microlenses, were fabricated on top of a supporting borosilicate glass with a thickness of 170 μm that is integral to the design of the system. Each microlens has the geometrical parameters reported in **Table I**.

2PP is intrinsically a slow fabrication method. In fact, 2PP structuring of the whole volume of a full microlens requires up to 12 hours. Therefore, we had two major requirements: first of all to speed up the production, and then to obtain an optical quality surface. In order to speed up the process and to match a reasonable prototyping time, we decided to two-photon polymerize the outer surface of each lens only (**Fig.2A**), and to subsequently expose to UV radiation the sample, in order to crosslink the unpolymerized photoresist within the volume by a bulk one-photon polymerization (**Fig.2B**) [16,26–28]. In addition, in order to provide high surface quality, the polymerization of the contour was carried out by a concentric circular scanning of the impinging laser beam around the lens axis (**Fig.2C**). Starting from the CAD design of the lens from Zemax calculations, we used a dedicated code to slice the model and to obtain a matrix of points in cartesian coordinates for each slicing plane. The G-code for the microfabrication has been defined as a sequence of concentric circles with a decreasing radius along the optical axis of the lens (**Fig.2C**). To smooth the outer surface, a good superposition of the polymerized circles has been obtained managing both the vertical step $\delta Z_{slicing}$ (typically $\delta Z_{slicing} <= 1\ \mu m$) and the planar step δR_{Raster} as the radius of each cycle ($\delta R_{Raster} <= 0.5\ \mu m$) relative to the curvature of the spherical surface (**Fig.2D**).

The fabrication process was carefully optimized to obtain the smoothest surface for the microlenses. In the first outcomes of fabrication, the spherical outer surface was affected by a visible hinge related to the start and end points of each polymerized circle (**Fig.2E-F**). Accordingly, we implemented in the code a random distribution of the start/end writing points within an angle of 120 degrees. The homogeneity of the outer surface increased, despite a

few regions of overexposure related to the writing acceleration and deceleration during the rotations (**Fig.2G-H**). To avoid this effect, we added a rotation without irradiating the photoresist before and after each polymerization cycle. The quality and the smoothness of the outer surface is visibly improved, even if the central region on the top plane of the lens is still affected by the very dense overlap of the polymerized lines resulting in an overexposed region. Therefore, according to the planar and vertical resolutions of the polymerization voxel, which are XY_{Voxel} ~ 1 µm and Z_{Voxel} ~ 5 µm respectively, the fabrication protocol was optimized by excluding a central area of the top of the lens with radius ~ 1 µm from the 2PP process. Still, some effect of the overexposure was present (**Fig.2H**). As literature evidence demonstrates, the complete homogeneity of the central part is a common and crucial issue related to the technique and the process of fabrication[27]. The top area polymerization was then optimized by slowly reducing the translation speed and laser power (1-2% in each step) in the last 2PP loops[29].

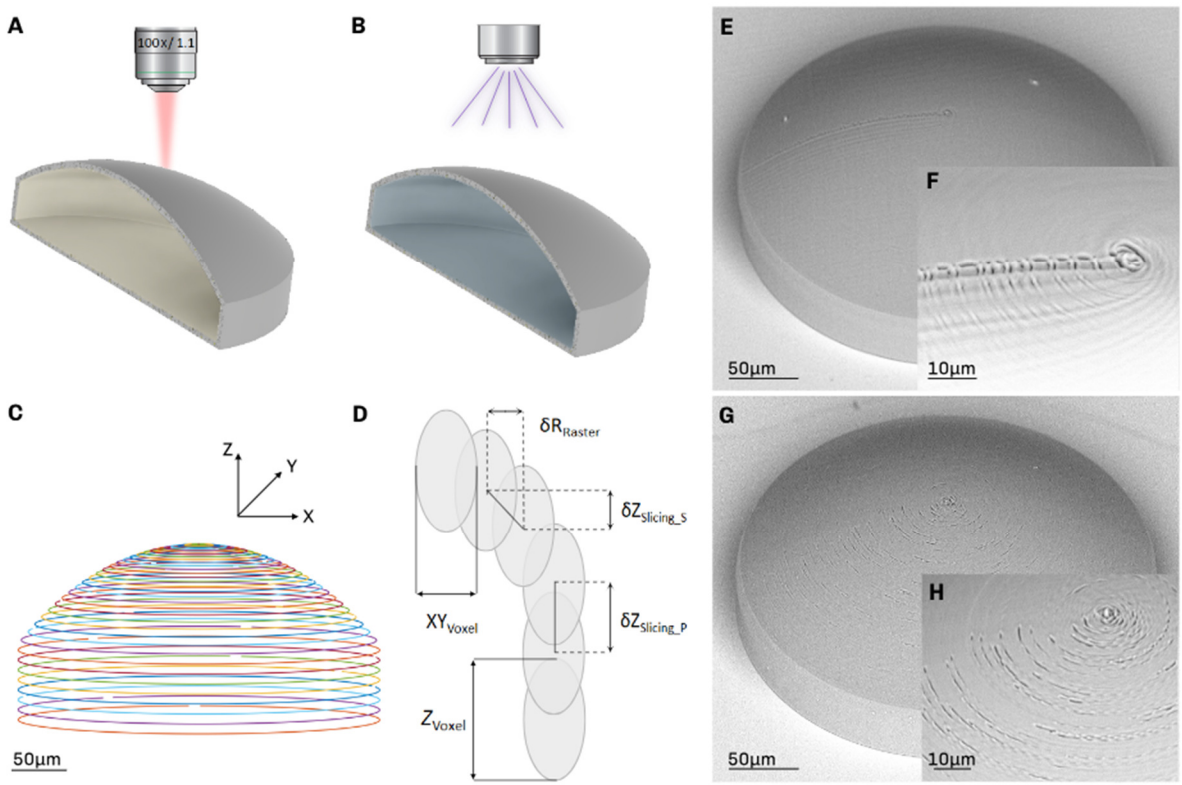

Figure 2. Scheme of the microlens fabrication protocol. **A**: 2PP of the lens outer surface focusing the laser beam with a 100x water immersion objective (NA 1.1). **B**: UV exposure to

crosslink the unpolymerized core of the lens. **C**: rendering of the outer shell of the microfabricated lens obtained from the G-code as a sequence of concentric cycles with decreasing radius along the optical axis of the lens. **D**: details of the contour parameters of rasterization and slicing on both the pedestal ($\delta Z_{Slicing_P}$) and spheric ($\delta Z_{Slicing_S}$, $\delta R_{_Raster}$) part of the lens, and three dimensional resolution of the polymerization voxel (XY_{voxel}, Z_{voxel}). **E**: SEM image of the first version of the microlens. **F**: detail of the hinge on the outer surface due to the same start Y coordinate at each rotation. **G**: SEM image of a microlens after the randomization of the distribution of the start/end points for each rotation. **H**: detail of the overexposure effect due to the acceleration and deceleration of the translation stages during laser irradiation (random start-end point within an angle of 120 degrees).

After the two-photon polymerization of the outer surface of the microlens, the surrounding unpolymerized photoresist was removed and then the core of the lens was cured by UV irradiation (see Materials and Methods).

In summary, the optimized fabrication protocol promotes a 98% reduction of the fabrication time, if compared to the one required to 2PP the whole volume of a full lens (from 12 hours to 8 minutes). At the same time, both slicing and radial steps, here employed, ($\delta Z_{slicing} = 1\ \mu m$; $\delta R_{Raster} = 0.5\ \mu m$) both the fabrication protocol we devised, allowed us to obtain a lens surface quality appropriate to perform optical imaging (as better shown in the optical characterization section) and with a good reproducibility ($\pm 5\%$) of the shape (see **SI 6, "Profilometer analysis of the shape of the microlenses"**). In addition, an even smoother surface can be obtained, by decreasing the imposed radial step to $\delta R_{Raster} \simeq 0.3\ \mu m$, during the polymerization at the expense of the fabrication time. Fabrication time increases from 8 minutes per lens at $\delta R_{Raster} \simeq 0.5\ \mu m$ to 15 minutes per lens at $\delta R_{Raster} \simeq 0.3\ \mu m$. Overall, we obtain stable microlenses with optical quality and with a higher size if compared with the microlenses fabricated by 2PP in the literature[16,26–28,30–32].

Our imaging area can be even increased with respect to the predicted $\simeq 250\ \mu m$ for a single microlens (**SI5, "Field of view of microlenses"**) by rescaling the microfabrication process to an hexagonal array of microlenses covering an area of $\simeq 800\ \mu m$ (**Fig.3B**). Four hexagonal arrays (**Fig.3C**) were fabricated on a 12mm Ø circular glass substrate (170 µm thickness)

covering an area 1.5 mm in side. The production of one set of arrays requires less than 4 hours.

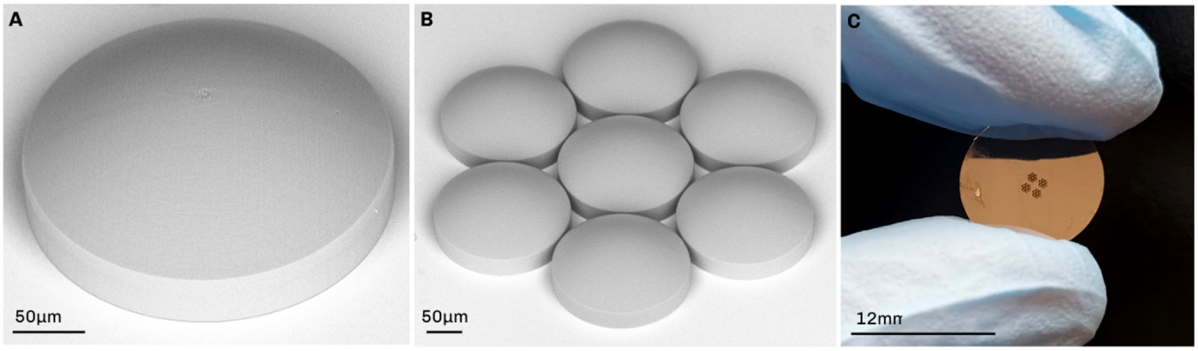

Figure 3. Final outcome of fabrication. **A**: SEM image of one microlens obtained from the optimization of the 2PP fabrication process and UV exposure. **B**: SEM image of one array of seven microlenses symmetrically set in a hexagonal configuration covering an area 800 µm in diameter. **C**: Image of a sample with 4 arrays of seven microlenses each covering an area 1.5 mm in side.

2.3 Optical characterization.

Before assessing the possibility to get fluorescence images of cells through the fabricated microlenses, we tested their optical quality by the study of the intensity distribution of a beam propagating along the optical axis, the wave front measurement at the focal plane and the measurement of the modulation transfer function. For all these tests, we used a collimated diode laser beam at $\lambda = 635\, nm$.

<u>Minimum spot size under collimated beam</u>. The intensity distribution on planes perpendicular to the optical axis provides a direct visualization of the effect of the aberrations, each having a peculiar signature[33]. The microlenses were tested in overfilling conditions to enhance the aberration effect. The intensity distributions sampled at $10\, \mu m$ steps (**Fig.4A** and **SI7, "Intensity distribution sampling along the optical axis"**) in a range of about $\pm 20\, \mu m$ around the effective focal plane of the microlens (corresponding to the minimum spot size) are reported in **Fig. 4B**. These images indicate the presence of spherical aberrations as concentric circles, turning more evident for distances $z < f_{FFL}$: for planes at distances larger than the front focal length, $z > f_{FFL}$, as expected[33], the central peak of the intensity distributions becomes more diffuse and the concentric rings cannot be singled out. The simulated intensity

distributions (**Fig.4C**) match very well the experimental ones. Due to the presence of the spherical aberration rings, we cannot define a Gaussian width $(1/e^2)$ for the intensity distribution across the optical axis (see also **SI7, "Intensity distribution sampling along the optical axis"**). However, the full width at half maximum (FWHM) of the central spot in planes close to the plane of minimum confusion can be measured on cross-section profiles of the intensity distributions. The full width, FWHM $= 0.96\,\mu m$, is in very good agreement with the simulation of the beam profile (**Fig.4D**). This value corresponds to a $1/e^2$ radius of $w_0 \simeq 0.82\,\mu m$. An estimate of the Rayleigh range, z_R, can be obtained by the relation $z_R = \pi {w^4}_0/\lambda \simeq 2.2\,\mu m$ at $\lambda = 0.635\,\mu m$. A direct measurement of the Rayleigh range is not straightforward due to the spherical aberrations. Their effect can be averaged out by computing the cumulative sum of the imaged Gaussian distributions[34] (see **SI7, "Intensity distribution sampling along the optical axis"**). By doing so, we obtain best fit values $z_R = 5.6 \pm 1.5\,\mu m$ that is approximately 2.5 times larger than the estimate done on the FWHM due to the presence of side lobes in the intensity distribution arising from the spherical aberrations.

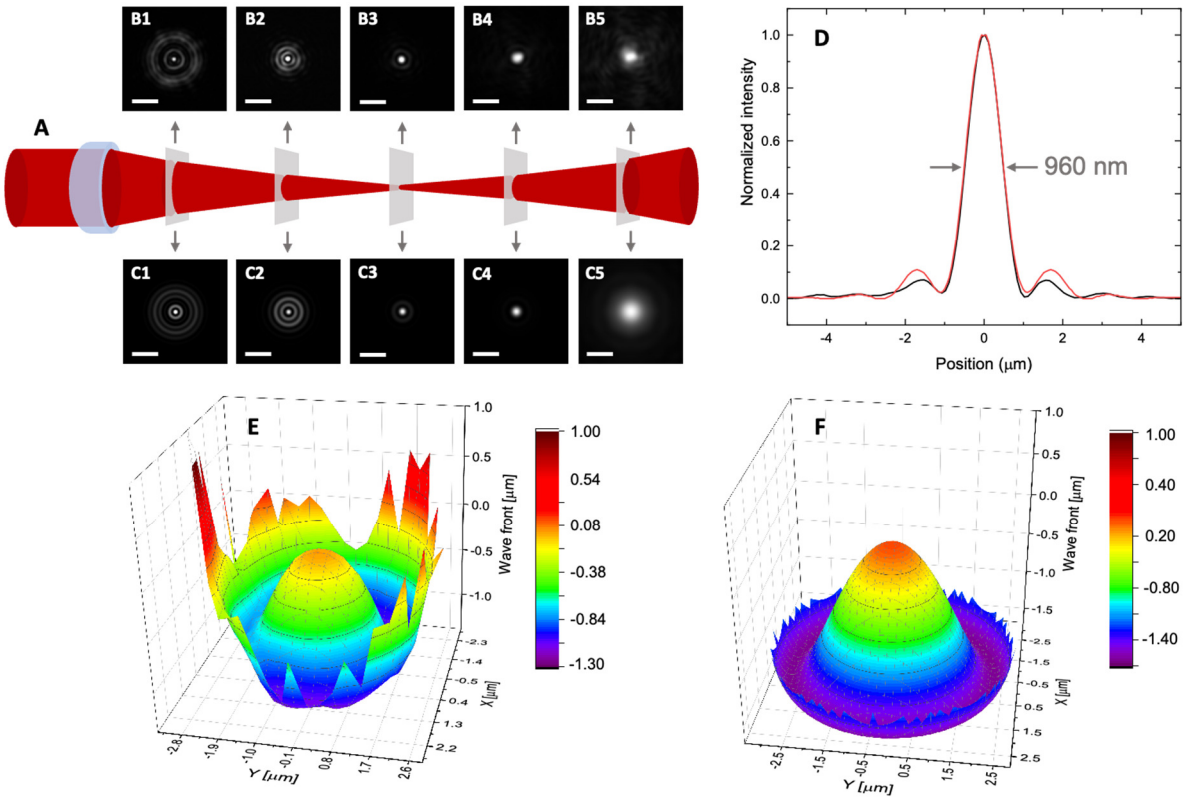

Figure 4. Aberrations of the microlenses. **A**: Schematics of the configuration adopted for the measurement of the intensity distribution of a Gaussian beam focused by a plano-convex microlens (Table I). The tube lens and the camera sensor are aligned to accept rays from infinite (see **SI8** for details). **B**: Images of the intensity profiles collected at various distances along the optical axis. The mutual distance between the planes is 10 µm, starting from the plane closer to the microlens (from left to right). Scale bars 5 µm. **C**: Simulated intensity distributions with the same 10-µm spacing along the optical axis. Scale bars 5 µm. **D**: Profile of a Gaussian beam focused by the microlens (the beam overfills the microlens with $1/e^2$ size = 9 mm). Experimental and simulated data are reported as black and red lines, respectively. $FWHM \simeq 960\,nm$. **E-F**: Wave front measured (**E**) and simulated (**F**) at the focal plane (minimum confusion plane) of the microlens. Piston, tip and tilt aberrations were subtracted from the experimental wavefront for visualization.

Wave front measurement. The wave front was measured by means of a Shack-Hartman sensor (WFS20-K1/M, Thorlabs, USA) with a 150 µm pitch array of lenses (**SI4**, "**Microlens wave front measurement**"). The wave front of the microlens, at the maximum pupil of about $264\,\mu m$ is reported in **Fig.4E**. The mexican-hat shape is characteristic of the $Z_{4,0}$ Zernike polynomial that characterizes the first order spherical aberration. The peak-to-valley value of the wave front, after subtraction of the piston and tilt components, is about $1.3\,\mu m$, similar to the simulated value (**Fig.4F**), $\simeq 1.7\,\mu m$. The Zernike decomposition of the experimental wave front gives an amplitude of the spherical component $a_{4,0} = 0.1\ \pm 0.01\,\mu m$. This value is similar to the result obtained on a 25 mm focal length plano-convex lens (Thorlabs, LA1252) at 33% pupil size (8.4 mm), $a_{4,0} = 0.17\ \pm 0.02\,\mu m$.

Modulation transfer function. The MTF can be measured point-wise by means of the analysis of a reference target, such as the USAF 1951. A qualitative result of the imaging of the USAF target through the microlenses is given in **Fig.5A-B**. The microlenses are used in a finite conjugate condition (**Fig.SI8.1A**), with a magnification determined by the ratio of the sample to entrance principal plane distance (p) over the exit principal plane to image plane distance (q). A 20x microscope objective collects the image produced by the microlens in the objective focal plane.

The MTF of the fabricated microlenses was derived by inserting a sharp edge in the sample plane, and by collecting and digitizing an image to retrieve the Edge Spread Function (ESF) (**Fig.5C**). After the subtraction of a wide low background, we computed the derivative of the

ESF to obtain the Line Spread Function (LSF), whose Fourier transform is the Modulation Transfer Function (MTF, **Fig.5D**). The MTF, that is the modulus of the Fourier Transform of the point spread function, offers a complete evaluation of the optical response of the microlenses for imaging purposes[35].

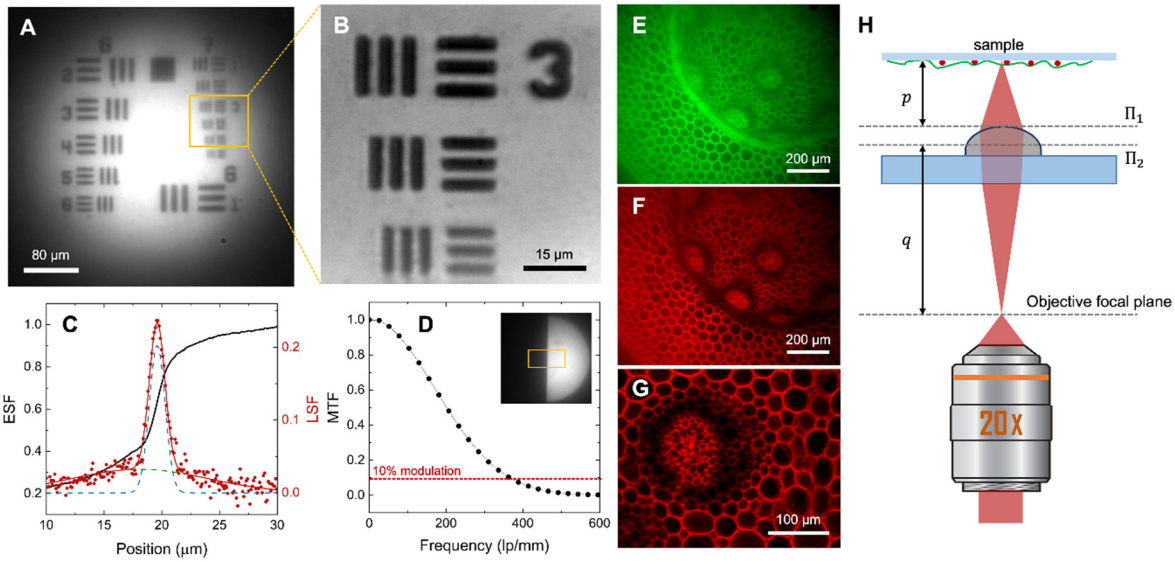

Figure 5. Optical performance of the microlenses. **A-B**: Example of widefield images of an USAF1951 resolution test chart obtained by a single microlens and a 20x objective as described in the text. Depending on the adopted relative positions of the microlens and the objective the overall magnification equals 6x (**A**) and 30x (**B**). **C**-**D**: Measurement of the MTF (Modulation Transfer Function) of the microlenses by the knife edge method. **C**: Edge Spread Function (ESF, black curve) and Line Spread Function (LSF, red curve) of a single microlens. **D**: MTF of the microlens derived as the Fourier transform of the LSF in panel **C**. Inset: Image of a sharp razor blade produced by the microlens and exploited for the ESF quantification. The ESF is extracted as the average intensity profile along the horizontal axis within the yellow Region of Interest; the LSF is computed as the first derivative of the ESF. **E-F**: Wide field images of a sample of Convallaria Majalis under blue (E) and green (F) epifluorescence excitation. **G:** Control wide field image of the same sample obtained on a confocal microscope (Methods section). **Panel H**: sketch of the finite conjugate use of the microlens. Π_1 and Π_2 are the two principal planes.

<u>Cell imaging through the microlenses.</u> As a proof of concept, microlenses can be coupled to a wide field microscope to collect wide field images both in transmission and in fluorescence mode, or can be coupled in a virtual image configuration to a scanning optical microscope (see **SI3, "Microlens coupling to microscopes"**). In the first case, the microlenses are used

in the same finite conjugate condition (**Fig.5H** and **SI8**) exploited for the USAF target imaging in **Fig.5**. Examples of fluorescence wide field images collected in this configuration are reported in **Fig.5E,F** for a sample of Convallaria Majalis, excited in the blue (**Fig.5E**) or the green (**Fig.5F**) spectral bands. From these images, very similar to the ones obtained using a confocal microscope **(Fig.5G**), we can clearly distinguish the most relevant parts of the root. The pericycle and endodermis appear as a bright green circle in **Fig. 5E**, surrounding a set of xylems and phloems and surrounded by the cortex. A slight field curvature can be observed at the edge of the field of view in **Figs.5E** and **5F**, compared to the reference image in **Fig.5G**. For non-linear excitation microscopy it is essential to couple the microlens with a scanning setup. In this second type of application, we couple the microlenses directly to a low numerical aperture objective in a raster scanning optical microscope. The microlens is set at a distance from the exit lens of the objective smaller than the objective working distance (see **Fig.6L** and **SI8**). In this configuration the microlens creates, for any position of the laser beam during the scanning, a virtual image of the sample that is then collected by the microscope objective (see **Fig.SI8.1B**). The magnification of the resulting image can be computed as the product of the magnification of the objective and that of the microlens. The latter depends directly on the distance, δz, between the microlens and the sample plane of the microscope objective (for details see **SI3,** "**Microlenses coupled to a raster scanning optical microscope**"). This configuration can be implemented both on confocal and on non-linear excitation fluorescence microscopes, also in the case of a microlens array as reported in **Fig.6**. In the example of **Fig.6**, the sample is a cell culture (human fibroblasts) grown on the very same glass slide (opposite side) on which the microlenses are fabricated. Fibroblasts are imaged at various degrees of magnification by changing the position of the microlens array with respect to the microscope objective. When $\delta z \simeq 0$, only the cells not covered by the microlenses can be imaged, with the microscope objective magnification (**Fig.6A** and **Fig.6D**). When $\delta z \simeq 165\ \mu m$, one can get images of the cells through the microlenses (**Fig.6B,C**). The estimated magnification due to the microlens (see **SI3,** "**Microlenses coupled to a raster scanning**

optical microscope") is $M_T \simeq 2.4$. 3D reconstruction of the cell culture is also possible as it is shown in **Fig.6E**.

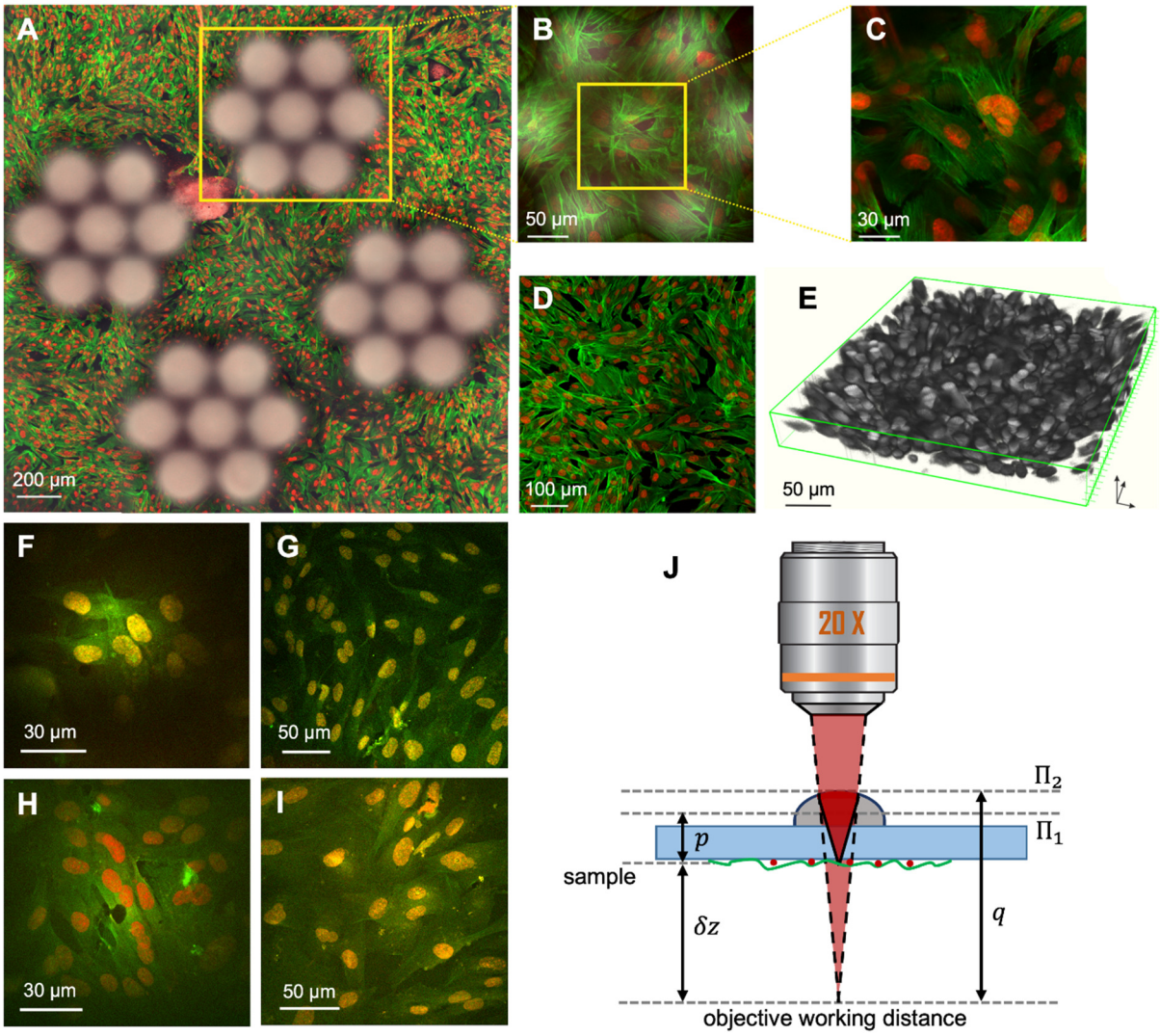

Figure 6. A: Confocal image (3x3 stitched tiles) of stained human fibroblasts (FITC-phallodin and DRAQ5 staining). The fluorescence confocal and transmitted images at the glass coverslip focal plane are superimposed. Microlenses are imaged through out-of-focus transmitted laser light. Cell nuclei, in red, and cytoskeleton, in green, are visualized in fluorescence (actin, excitation at 488 nm, emission at 525/50 nm; nuclei, excitation at 561 nm, emission at 593/46 nm). **B**: Full field-of-view fluorescence confocal image through an array of microlenses, superimposed to the transmitted-light image. The cell fluorescence image is collected when the sample is shifted by $\delta z = 165\ \mu m$ with respect to the objective focal plane. **C**: Cropped scan area through a single microlens. **D**: Full field-of-view confocal microscope image of cells at the glass coverslip focal plane ($\delta z \simeq 0$, scale bar $100 \mu m$). A 20x dry objective was employed for **A-D**. **E**: 3D reconstruction of cells through an array of microlenses. The image was rescaled accordingly to the microlenses magnification: $M_T \simeq 2.4, M_z \simeq {M_T}^2$. **F-I:** Fluorescence images of the cells under two-photon excitation ($\lambda = 800 nm$). Nuceli are stained with Hoechst. **F**: Fluorescence image collected through the microlenses coupled to a 20x dry objective at a distance $\delta z = 135\ \mu m$ (with respect to the objective sample plane), resulting in a total magnification $M_{tot} \simeq 45$. **G**: Control image obtained through the 20x dry objective at

$\delta z \simeq 0$. **H**: Image of the cells through the microlenses coupled to a 25x water immersion objective obtained at $\delta z \simeq 43\,\mu m$. **I:** Control image obtained with the 25x water immersion objective when $\delta z \simeq 0$. **Panel J**: sketch of the configuration used to couple the microlens with the optical scanning microscope. The distance between the sample (dark gray) and its virtual image (light gray) through the microlens is δz. Π_1 and Π_2 are the two principal planes of the microlens.

Notably, the resolution and the signal to noise ratio of the images collected through the microlenses are very similar to the ones obtained on the confocal microscope itself. Moreover, we can verify that the microlens optical quality is sufficient to induce two-photon excitation and to collect non-linear excitation fluorescence images both when used in air (**Fig.6F**) and when used with water immersion objectives (**Fig.6H**), despite the lower dioptric power of the microlenses, due to partial index matching. When the microlenses are coupled with a 20X dry microscope objective we found that the images of the cells through the microlenses can be recovered at $\delta z = 135\,\mu m$ resulting in a magnification $\simeq 2.3$, that leads to a total magnification of $M_{tot} = M_T\, M_{obj} \simeq 2.3 \times 20 \simeq 46$. When the microlenses are coupled to a 25X water immersion objective, the images of the cells through the microlenses can be recovered at $\delta z = 43\,\mu m$, corresponding to a magnification $M_T \simeq$1.75, that leads to a total magnification of $M_{tot} = M_T\, M_{obj} \simeq 1.75 \times 25 \simeq 44$. Indeed the raster scanning images obtained with the two microscope objectives are quite similar. The field of view is reduced by a three/fourfold factor, with respect to the FOV of the objectives, depending on the coupling distance between the microlenses and the objective.

Conclusions.

In summary, we have shown that microlenses can be fabricated with a high throughput, about 8 minutes/lens, by limiting the 2PP fabrication to a $\simeq 1\,\mu m$ thick outer crust and a post-development volume polymerization. This procedure leads to a 98% reduction in the fabrication time with respect to volume polymerization, still obtaining sufficient optical quality to use the lenses for direct wide field imaging of cells, both in transmission and in fluorescence

mode. No evidence of inhomogeneities in the lens volume is found due to the post-development processing.

Wide field imaging through the microlenses can be obtained in a finite conjugate coupling approach, where the microscope objective and the microlenses are arranged in series. This method can be used for routine testing of the optical quality of the microlenses. More interesting, the microlenses can be coupled to a raster scanning non-linear excitation optical microscope, even by using low numerical aperture and low magnification objectives: in this case a virtual image configuration is adopted. Our experiments (**Fig.6**) show for the first time that it is possible to use the microfabricated microlenses to efficiently induce non-linear excitation and collect two-photon excitation images from cells with the same level of laser intensity and similar signal to noise ratio. This work opens the possibility to implement micro-optical devices for nonlinear excitation that, due to the limited size, could be used as implants for the direct and continuous optical inspection of biological dynamics *in vivo*.

MATERIALS and METHODS

Sample Preparation for Two-Photon Laser Polymerization:
The photoresist used for the 2PP of the microlenses was a negative hybrid organic-inorganic UV-curable resist known as SZ2080TM[36], biocompatible and validated for biological applications[6,37]. To increase the efficiency of the polymerization 1% of Irgacure-369 (2-Benzyl-2-dimethylamino-1-(4-morpholinophenyl)-butanone-1) is added to the resist as photoinitiator. About 46 µl of liquid SZ2080 photoresist were deposited by drop casting on a 12 mm diameter circular glass coverslip with a thickness between 170 and 230 µm (#1.5, Menzel-Glaser, Germany). To allow the drying of the resist thus to prevent any unwanted sliding of the structures during the fabrication process, the samples were left under the chemical hood for 48 hours. Once the material had condensed, the photoresist reached a semi-solid state suitable for the further laser-induced polymerization.

Two-Photon Laser Polymerization Setup:
The 2PP fabrication was performed by a femtosecond Ytterbium (Yb) fiber laser (Satsuma, Amplitude System). The laser wavelength was 1030 nm, the pulse duration is ~280 fs and the repetition rate was fixed to 1MHz. The output power reaches a maximum value of 10 W . The laser beam passed through a series of mirrors that steered it to a 2x telescope and a half-wave plate coupled to a polarizer (MPS50GR-TTM-G80-DC-LMO-PLOTS, Aerotech, USA) which was used as a system for the power control. The half-wave plate was mounted on a software controlled motorized rotator which allows the dynamic control of the power during 2PP. At the end of the optical path the beam was tightly focused by a water matched CFI plan 100XC W objective with a numerical aperture (NA) 1.1 (Nikon, Japan) directly onto the photosensitive resist. The sample was mounted within a glass container with a diameter of 100 mm connected to a gimbal mechanical system (Gimbal Mounts 100, Thorlabs). The sample holder-gimbal complex was screwed on a planar (X, Y) translational stage (ANT95-50-XY, Aerotech, USA) while the motion of the objective along the Z-direction was controlled by a high resolution linear stage (ANT130-035-L-ZS, Aerotech, USA) balanced by two air compressed pneumatic pistons. The motion of this three-axes stages was controlled by software (Automation 3200 CNC Operator Interface, Aerotech, USA) as well as the half-wave plate rotation and they were provided with a feedback position and velocity control system with a resolution on the order of 200 nm. For a real time monitoring of the writing process within the working area, as well as the polymerization process, a red-light emitting diode illumination was positioned in the empty central cavity of the gimbal, under the sample holder-gimbal complex, and a CCD camera was mounted behind a dichroic mirror (Thorlabs, Germany). The three translational stages and all the components of the optical path were placed upon a granite table (Zali Precision Granite Technology, Italy).

The outer surface of each microlens was two-photon polymerized directly focusing the laser beam into the SZ2080 photoresist droplet, moving the sample at a speed of 1 mm/s. Due to laser radiation absorption, the pulse energy used for 2PP of the microlenses depends on the SZ2080 droplet thickness thus ranging from 13 nJ to 15 nJ.

Sample Development and UV Exposure:

After the two-photon polymerization process, the samples underwent a development procedure to remove the unpolymerized photoresist surrounding the volume of the microfabricated microlenses. The samples were soaked in a glass beaker filled with a 50% v/v 2-pentanone, 50% v/v isopropyl alcohol solution (Sigma-Aldrich, USA). After 30 min, they were cautiously washed with a few drops of isopropyl alcohol then gently dried by room temperature Nitrogen. Afterwards, the sample was UV irradiated passing through the glass substrate in order to avoid the direct and additional exposure of the previously polymerized surface. Consequently thus the radiation intensity and the time of exposure depend on the thickness of the substrate, the volume of photoresist to be polymerized and the shape of the lens. Therefore, the process was optimized exposing the sample to 300 mW of UV irradiation (λ=385nm) for 120 seconds (LIGHTNINGCURE LC-L1V3) in order to crosslink the unpolymerized core of the lens achieving the structural stability without causing resin degradation.

Optical and Scanning Electron Microscopy Qualitative Characterization:
Qualitative analysis of fabrication outcomes in terms of shape and mechanical stability were performed by an optical microscope with different magnitudes 4×, 10×, 20×, 40× (Eclipse ME600, Nikon, Japan) and by a scanning electron microscope (SEM, Phenom Pro, Phenom World, Netherlands). The SEM observations were carried out at 10 kV.

Profilometry Analysis:
The analysis of the overall shape of the lenses were performed by a surface profilometer (KLA Tencor P-17) using a 2.5 um stylus tip radius and setting the scan speed as 20 µm/s, 20 Hz sampling rate, 1 mg as the down force to be applied on the sample surface. The scanning of each lens was performed sampling it each 5 µm along both the planar directions (X,Y) and both the positive and negative sense, within a scanning box of 350 µm side. Lastly, the surface profile has been interpolated with a spheric function in order to evaluate the reliability of the fabrication with respect to the lens model.

Fluorescence microscopy:
For confocal imaging human dermal RFP fibroblasts (Innoprot, Spain) were cultured in Dulbecco's modified Eagle's medium (DMEM) supplemented with 10% fetal bovine serum, 1% L-glutamine (2 mM), penicillin (10 units/ml),and streptomycin (10 µg/ml) at 37℃ and 5% CO2 . Then, 20k/50µl cells were drop-seeded on borosilicate glass coverslips,and after 4 hours of incubation, diluted in 3 ml of DMEM and expanded for 48 hours. Then, cell culture was fixed in 4% paraformaldehyde (Sigma Aldrich, Italy) for 5 minutes and stained, for nuclei identification, with: DRAQ5 (ThermoFisher Scientific, Italy) in a dilution ratio of 1:1000 in PBS for 15 minutes and with 1 µg/ml Hoechst 33342 (ThermoFisher Scientific, Italy) for 10 minutes at room temperature. Finally cells were incubated for 45 minutes with 1 µg/ml of FITC-phalloidin (Sigma Aldrich, Italy), to stain actin cytoskeleton. The images were taken on a A1R+ Nikon (Nikon, Japan) confocal microscope equipped with an apochromat, 20X, NA 0.8 dry objective lens. Images were taken by exciting at λ =488 nm for actin filaments stained with FITC (emission collected through a 525/50 nm band pass filter) and at λ =561 nm for nuclei stained with DRAQ5 (emission collected through a 593/46 nm band pass filter).
Wide-field fluorescence images were taken on a Leica SP5 microscope equipped with a 20X dry objective (HC PL Fluotar, NA=0.5). Phase-contrast images were taken with a 4X, NA 0.13, dry objective on an Olympus IX70 inverted optical microscope.

Two-photon excitation fluorescence microscopy:
Two photon fluorescence microscopy was performed on a custom setup based on a BX51 (Olympus, Japan) direct microscope equipped with either a water immersion long working distance objective (XL Plan N, 25X, NA=1.05, Olympus, Japan) or a dry objective (Plan N, 20X, NA=0.4, Olympus, Japan). The raster scanning images were acquired through a M610 (ISS Inc., Urbana-Champaign, USA) scanning head coupled to a Ti:Sapph laser (MaiTai DeepSee, Newport, USA) and to two analog photomultiplier tubes ((HC125-02, Hamamatsu, Japan).

Optical characterization of microlenses.
In all the optical characterization the source was a fiber coupled 635 nm laser diode (HLS635 + P1-630A-FC-1 single mode fiber) collimated by a plan 4X, NA=0.10 objective (Olympus, Japan).
Wave front measurements. The wave front was measured by means of a Shack-Hartman sensor (WFS20-K1/M, Thorlabs, USA) with a 150 µm pitch array of lenses. A planar Gaussian beam overfills the microlens pupil to be tested. Part of the beam is focused by the microlens on the focal plane of a 63X dry objective that collimates it at its exit pupil (**Fig.SI4.1**). A 4f telescope conjugates the electric field from the objective exit pupil plane magnifying it on the entrance pupil of the Shack-Hartman sensor. The fraction of the light that is not captured by the microlens is filtered at the intermediate plane of the 4f telescope by a pinhole (**Fig.SI4.1**), to single out only the wave front of the beam focused by the microlens.

Beam profile test. The minimum spot size that can be obtained through the microlenses was measured on an infinity conjugated microscope. The tube lens and the camera sensor (UI-1542LE-M, IDS, Obersulm, D) were carefully aligned to accept rays from infinity, so that the microscope objective collects the electric field in its front focal plane. The images collected by the camera at various positions of the focal plane of the objective give us the shape of the intensity profile generated by the microlenses.

Acknowledgments.
This research has received funding from the European Union under the Horizon 2020 research and innovation program (G.A. No. 964481 – IN2SIGHT).

Bibliography.

1 F. Mingozzi, R. Spreafico, T. Gorletta, C. Cigni, M. Di Gioia, M. Caccia, L. Sironi, M. Collini, M. Soncini, M. Rusconi, U. H. von Andrian, G. Chirico, I. Zanoni and F. Granucci, *EMBO Mol. Med.*, 2016, **8**, 1039–1051.

2 D. U. Pizzagalli, A. Pulfer, M. Thelen, R. Krause and S. F. Gonzalez, *Front. Immunol.*, 2022, 12.

3 E. Dondossola and P. Friedl, *Nat. Rev. Mater.*, 2022, **7**, 6–22.

4 E. Dondossola, B. M. Holzapfel, S. Alexander, S. Filippini, D. W. Hutmacher and P. Friedl, *Nat. Biomed. Eng.*, 2017, **1,7**, 1–10.

5 C. Prunier, N. Chen, L. Ritsma and N. Vrisekoop, *Methods*, 2017, **128**, 52–64.

6 C. Conci, E. Jacchetti, L. Sironi, L. Gentili, G. Cerullo, R. Osellame, G. Chirico and M. T. Raimondi, *Adv. Opt. Mater.*, 2022, **2101103**, 1–12.

7 Kenry, Y. Duan and B. Liu, *Adv. Mater.*, , DOI:10.1002/ADMA.201802394.

8 W. R. Zipfel, R. M. Williams and W. W. Webb, *Nat. Biotechnol.*, 2003, 21, 1369–1377.

9 V. Ntziachristos, *Nat. Methods*, 2010, **7**, 603–614.

10 F. P. Bolin, L. E. Preuss, R. C. Taylor and R. J. Ference, *Appl. Opt.*, 1989, **28**, 2297.

11 C. N. LaFratta, J. T. Fourkas, T. Baldacchini and R. A. Farrer, *Angew. Chemie - Int. Ed.*, 2007, 46, 6238–6258.

12 E. Skliutas, M. Lebedevaite, E. Kabouraki, T. Baldacchini, J. Ostrauskaite, M. Vamvakaki, M. Farsari, S. Juodkazis and M. Malinauskas, *Nanophotonics*, 2021, 10, 1211–1242.

13 A. Zeynali, M. Marini, G. Chirico, M. Bouzin, M. Borzenkov, L. Sironi, L. D'Alfonso, P. Pallavicini, V. Cassina, F. Mantegazza, F. Granucci, L. Marongiu, D. Polli, A. De la Cadena and M. Collini, *Adv. Opt. Mater.*, 2020, **8**, **2000584**, 1–11.

14 M. Bouzin, A. Zeynali, M. Marini, L. Sironi, R. Scodellaro, L. D'alfonso, M. Collini and G. Chirico, *Sensors*, 2021, 21, 1–36.

15 M. Marini, A. Zeynali, M. Collini, M. Bouzin, L. Sironi, L. D'Alfonso, F. Mantegazza, V. Cassina and G. Chirico, *Lab Chip*, , DOI:10.1039/D2LC00697A.

16 R. Guo, S. Xiao, X. Zhai, J. Li, A. Xia and W. Huang, *Opt. Express*, 2006, **14**, 810.

17 J. Li, P. Fejes, D. Lorenser, B. C. Quirk, P. B. Noble, R. W. Kirk, A. Orth, F. M. Wood, B. C. Gibson, D. D. Sampson and R. A. McLaughlin, *Sci. Rep.*, 2018, **8**, 1–9.

18 T. Gissibl, S. Thiele, A. Herkommer and H. Giessen, *Nat. Photonics*, 2016, **10**, 554–560.

19 T. Gissibl, S. Thiele, A. Herkommer and H. Giessen, *Nat. Commun.*, , DOI:10.1038/ncomms11763.

20 M. F. Griffin, H. E. desJardins-Park, S. Mascharak, M. R. Borrelli and M. T. Longaker, *Dis. Model. Mech.*, 2020, **13**, 1–9.

21 M. A. May, N. Barré, K. K. Kummer, M. Kress, M. Ritsch-Marte and A. Jesacher, *Nat. Commun.*, , DOI:10.1038/s41467-021-24666-9.

22 I. N. Papadopoulos, J. S. Jouhanneau, J. F. A. Poulet and B. Judkewitz, *Nat. Photonics*, 2017, **11**, 116–123.

23 V. Lakshminarayanan and A. Fleck, *J. Mod. Opt.*, 2011, **58**, 545–561.

24 M. V. Klein and T. E. Furtak, *Optics*, J. Wiley &Sons, New York, 2nd edn., 1991.

25 A. Žukauskas, G. Batavičiute, M. Ščiuka, Z. Balevičius, A. Melninkaitis and M. Malinauskas, *Opt. Mater. (Amst).*, 2015, **39**, 224–231.

26 M. Malinauskas, A. Žukauskas, V. Purlys, K. Belazaras, A. Momot, D. Paipulas, R. Gadonas, A. Piskarskas, H. Gilbergs, A. Gaidukevičiūtė, I. Sakellari, M. Farsari and S. Juodkazis, *J. Opt.*, 2010, **12**, 124010.

27 M. Malinauskas, H. Gilbergs, A. Žukauskas, V. Purlys, D. Paipulas and R. Gadonas, *J. Opt.*, 2010, **12**, 035204.

28 D. Wu, S.-Z. Wu, L.-G. Niu, Q.-D. Chen, R. Wang, J.-F. Song, H.-H. Fang and H.-B. Sun, *Appl. Phys. Lett.*, 2010, **97**, 031109.

29 T.-T. Chung, Y.-T. Tu, Y.-H. Hsueh and S.-Y. Chen, *Int. J. Autom. Smart Technol.*, 2013, **3**, 131–135.

30 D. Gonzalez-Hernandez, S. Varapnickas, G. Merkininkaitė, A. Čiburys, D. Gailevičius,

S. Šakirzanovas, S. Juodkazis and M. Malinauskas, *Photonics*, 2021, **8**, 577.
31 J.-G. Hua, H. Ren, A. Jia, Z.-N. Tian, L. Wang, S. Juodkazis, Q.-D. Chen and H.-B. Sun, *Opt. Lett.*, 2020, **45**, 636.
32 Y. Hu, Y. Chen, J. Ma, J. Li, W. Huang and J. Chu, *Appl. Phys. Lett.*, 2013, **103**, 141112.
33 M. Born and E. Wolf, *Principles of Optics*, Pergamon Press, 1959.
34 M. Bouzin, G. Chirico, L. D'Alfonso, L. Sironi, G. Soavi, G. Cerullo, B. Campanini and M. Collini, *J. Phys. Chem. B*, 2013, **117**, 16405–16415.
35 X. Zhang, T. Kashti, D. Kella, T. Frank, D. Shaked, R. Ulichney, M. Fischer and J. P. Allebach, in *Image Quality and System Performance IX*, SPIE, 2012, vol. 8293, p. 829307.
36 A. Ovsianikov, J. Viertl, B. Chichkov, M. Oubaha, B. MacCraith, I. Sakellari, A. Giakoumaki, D. Gray, M. Vamvakaki, M. Farsari and C. Fotakis, *ACS Nano*, 2008, **2**, 2257–2262.
37 M. T. Raimondi, S. M. Eaton, M. Laganà, V. Aprile, M. M. Nava, G. Cerullo and R. Osellame, *Acta Biomater.*, 2013, **9**, 4579–4584.